High-Order Discontinuous Galerkin Mesh Resolved Turbulent Flow Simulations of a NACA 0012 Airfoil

Michael J. Brazell * Dimitri J. Mavriplis †

A parallel high-order Discontinuous Galerkin (DG) method is used to simulate turbulent flow over a NACA 0012 airfoil. Using a family of high-density grids (available on the NASA turbulence modeling resource website) mesh resolved solutions are obtained. The flow is simulated by solving the Reynolds-Averaged Navier-Stokes equations closed by the negative Spalart-Allmaras turbulence model. The flow conditions for this case are: $\alpha = 10$, $M = .15$, and $Re = 6 \times 10^6$. Lift, drag, pitching moment, pressure, and skin friction coefficients are provided for multiple grids and discretization orders and compared against other simulation results from the CFL3D and FUN3D solvers. The DG simulations give very similar results to these solvers and which further verifies both the DG solver and the other methods as having mesh resolved solutions. Also, it is shown that p-refinement converges quicker to the mesh resolved solutions compared to h-refinement.

I. Introduction

Achieving higher accuracy and fidelity in aerodynamic simulations using higher-order methods has received significant attention over the last decade. High-order methods are attractive because they provide higher accuracy with fewer degrees of freedom and at the same time relieve the burden of generating very fine meshes. Discontinuous Galerkin (DG) methods[1] have received particular attention for aerodynamic problems; these methods combine the ideas of finite element and finite volume methods allowing for high-order approximations and geometric flexibility. The DG solver used in this work incorporates many of the techniques previously demonstrated by our group and others in the two-dimensional setting.[2–4] It supports hybrid, mixed-element, unstructured meshes including arbitrary combinations of tetrahedra, prisms, pyramids, and hexahedra. The solver has been designed to incorporate both p-enrichment and h-refinement capabilities using non-conforming elements (hanging nodes).[5]

The goal of this work is to use a three-dimensional high-order DG method to simulate flow over the NACA 0012 airfoil for cases taken from the NASA turbulence modeling resource website. A family of high-density grids is provided and are used to find mesh resolved solutions. These solutions are compared to other simulation data also provided on the turbulence modeling resource website. In the following sections, the governing equations are described, followed by the DG discretization and its implementation. The solution methodology is described next and is followed by a discussion of the simulation results of the NACA 0012 airfoil.

II. Governing Equations

The Navier-Stokes equations govern the dynamics of compressible fluids and are given as:

$$\frac{\partial U_m}{\partial t} + \frac{\partial F_{mi}}{\partial x_i} = 0 \tag{1}$$

where they represent the conservation of mass, momentum, and energy. The solution vector U and flux F are defined as:

*Post Doctoral Research Associate, Dept of Mechanical Engineering, University of Wyoming
†Professor, Dept of Mechanical Engineering, University of Wyoming

$$U = \begin{Bmatrix} \rho \\ \rho u_1 \\ \rho u_2 \\ \rho u_3 \\ \rho E \end{Bmatrix}, \quad F = \begin{Bmatrix} \rho u_1 & \rho u_2 & \rho u_3 \\ \rho u_1^2 + P - \tau_{11} & \rho u_1 u_2 - \tau_{12} & \rho u_1 u_3 - \tau_{13} \\ \rho u_1 u_2 - \tau_{21} & \rho u_2^2 + P - \tau_{22} & \rho u_2 u_3 - \tau_{23} \\ \rho u_1 u_3 - \tau_{31} & \rho u_2 u_3 - \tau_{32} & \rho u_3^2 + P - \tau_{33} \\ \rho u_1 H - \tau_{1j} u_j + q_1 & \rho u_2 H - \tau_{2j} u_j + q_2 & \rho u_3 H - \tau_{3j} u_j + q_3 \end{Bmatrix} \tag{2}$$

where ρ is the density, u_i are the velocity components in each spatial coordinate direction, P is the pressure, E is total internal energy, $H = E + P/\rho$ is the total enthalpy, τ is the viscous stress tensor, and q is the heat flux. The viscous stress tensor and heat flux are defined as:

$$\tau_{ij} = (\mu + \mu_t) \left(\frac{\partial u_i}{\partial x_j} + \frac{\partial u_j}{\partial x_i} - \frac{2}{3} \delta_{ij} \frac{\partial u_k}{\partial x_k} \right)$$

$$q_i = -\gamma \left(\frac{\mu}{Pr} + \frac{\mu_t}{Pr_t} \right) \left(\frac{\partial E}{\partial x_i} - u_j \frac{\partial u_j}{\partial x_i} \right)$$

where Pr and Pr_t are the Prandtl and turbulent Prandtl numbers, μ is the dynamic viscosity, and μ_t is the dynamic eddy viscosity. The dynamic eddy viscosity is only active when using a turbulence model which is described in the next section. The viscosity μ is a function of the constant viscosity μ_0 and the temperature given by the Sutherland's formula:

$$\mu = \mu_0 \left(\frac{RT}{RT_0} \right)^{3/2} \left(\frac{RT_0 + RC}{RT + RC} \right).$$

The gas constant R is multiplied in all of the terms so that it never has to be defined and $RT = P/\rho$ is used instead. In the Sutherland formula C is a scaled Sutherland constant defined as:

$$RC = \frac{S}{T_{ref}} RT_0$$

where $S = 110.\bar{3}K$ is the standard Sutherland constant, $T_{ref} = 300K$ is the reference temperature, and $RT_0 = P_0/\rho_0$ is the initial temperature. These equations are closed using the ideal gas equation of state:

$$\rho E = \frac{P}{\gamma - 1} + \frac{1}{2} \rho (u_1^2 + u_2^2 + u_3^2)$$

where γ is the ratio of specific heats. In all of the following, Einstein notation is used where the subscripts of i, j, and k represent spatial dimensions and have a range of 1 to 3 and the indices of m and n vary over the number of variables.

III. Negative Spalart-Allmaras

Under turbulent flow conditions the compressible Navier-Stokes equations shown in the previous section can be used to solve the Reynolds Averaged Navier Stokes equations. This is done by adding a dynamic eddy viscosity μ_t to the viscous flux. The dynamic eddy viscosity is defined as:

$$\mu_t = \begin{cases} \mu' \rho \nu_t f_{v1} & \nu_t \geq 0 \\ 0 & \nu_t < 0 \end{cases}$$

where $\mu' = 1000\mu_0$ is a scaling constant,

$$f_{v1} = \frac{\chi^3}{\chi^3 + c_{v1}^3}, \quad \chi = \frac{\mu' \rho \nu_t}{\mu}$$

and ν_t is the rescaled kinematic eddy viscosity, or the SA working variable. The variable is solved using the one-equation Spalart-Allmaras (SA) turbulence model.[6] The negative variant of the SA model is used in this work and is given by the transport equation:

$$\frac{\partial \rho \nu_t}{\partial t} + \frac{\partial \rho \nu_t u_i}{\partial x_i} - \frac{1}{\sigma} \frac{\partial}{\partial x_i} \left[(\mu + \mu' f_n \rho \nu_t) \frac{\partial \nu_t}{\partial x_i} \right] = \rho (P - D) + \frac{\mu' c_{b2} \rho}{\sigma} \frac{\partial \nu_t}{\partial x_i} \frac{\partial \nu_t}{\partial x_i} - \frac{1}{\sigma} \left(\frac{\mu}{\rho} + \mu' \nu_t \right) \frac{\partial \rho}{\partial x_i} \frac{\partial \nu_t}{\partial x_i}. \tag{3}$$

All of the terms are described below because of the scaling factor μ' that is introduced. This scaling factor cane be used to improve the convergence rate of the implicit Newton-Krylov DG-solver.[7] The trip terms are not implemented so are eliminated from the equation. In the negative-SA model the production and destruction terms depend on the sign of the eddy viscosity and are defined as:

$$P = \begin{cases} c_{b1}\left(1 - f_{t2}\right)\tilde{s}\nu_t & \nu_t \geq 0 \\ c_{b1}\left(1 - c_{t3}\right)s\nu_t & \nu_t < 0 \end{cases}, \quad D = \begin{cases} \mu'\left(c_{w1}f_w - \frac{c_{b1}}{\kappa^2}f_{t2}\right)\left(\frac{\nu_t}{d}\right)^2 & \nu_t \geq 0 \\ -\mu' c_{w1}\left(\frac{\nu_t}{d}\right)^2 & \nu_t < 0 \end{cases}$$

where s is the magnitude of vorticity:

$$s = \sqrt{\omega_i \omega_i},$$

$\tilde{s}$ is the modified vorticity:

$$\tilde{s} = \begin{cases} s + \bar{s} & \bar{s} \geq -c_{v2}s \\ s + \frac{s\left(c_{v2}^2 s + c_{v3}\bar{s}\right)}{\left(c_{v3} - 2c_{v2}\right)s - \bar{s}} & \bar{s} < -c_{v2}s \end{cases},$$

$$\bar{s} = \frac{\mu'\nu_t f_{v2}}{\kappa^2 d^2}, \quad f_{v2} = 1 - \frac{\chi}{1 + \chi f_{v1}},$$

and d is the distance to the closest wall. The function f_n and the laminar trip term f_{t2} are defined as:

$$f_n = \frac{c_{n1} + \chi^3}{c_{n1} - \chi^3}, \quad f_{t2} = c_{t3}e^{-c_{t4}\chi^2},$$

and the function f_w is defined as:

$$f_w = g\left[\frac{1 + c_{w3}^6}{g^6 + c_{w3}^6}\right]^{1/6}, \quad g = r + c_{w2}\left(r^6 - r\right), \quad r = \min\left(\frac{\mu'\nu_t}{\tilde{s}\kappa^2 d^2}, r_{lim}\right).$$

Lastly, the constants are $\sigma = 2/3$, $c_{b1} = 0.1355$, $c_{b2} = 0.622$, $\kappa = 0.41$, $c_{w1} = c_{b1}/\kappa^2 + \left(1 + c_{b2}\right)\sigma$, $c_{w2} = 0.3$, $c_{w3} = 2$, $c_{v1} = 7.1$, $c_{v2} = 0.7$, $c_{v3} = 0.9$, $c_{t1} = 1$, $c_{t2} = 2$, $c_{t3} = 1.2$, $c_{t4} = 0.5$, $r_{lim} = 10$, $c_{n1} = 16$. The negative SA transport equation shown in Equation 3 is fully coupled to the compressible Navier-Stokes equations. Also, the terms on the right hand side are treated as source terms.

IV. DG Formulation

In this section the DG finite element formulation used to solve the Navier-Stokes equations is described. A crucial part to any finite element method is the choice of basis. Two sets of basis functions have been implemented for all types of elements (tetrahedra, pyramid, prism, and hexahedra). The first is a C^0 hierarchal modal basis and the second is a orthonormal hierarchal modal basis. The basis for the solution and the basis for the geometrical mapping can be independently chosen. Also, each element can have a different polynomial degree for the solution and geometrical mapping. For example, the orthonormal basis can be chosen for the solution and the C^0 basis for the geometrical mapping. Also, the solution can have a polynomial degree of $p = 4$ while the mapping could have a polynomial degree of $p = 1$, or the mapping could have a polynomial degree of $p = 5$ which could be used for curved boundaries. In this work the orthonormal basis is used and the polynomial degree of mapping basis is always chosen to be one degree higher than the polynomial degree of the solution basis.

To derive the weak form, equation (1) is first multiplied by a test function ϕ and integrated over the domain Ω to give:

$$\int_\Omega \phi_r \left(\frac{\partial U_m}{\partial t} + \frac{\partial F_{mi}}{\partial x_i} - S_m\right) \mathrm{d}\Omega = 0.$$

To obtain the weak form, integration by parts is performed and the residual R_{mr} is defined as:

$$R_{mr} = \int_\Omega \left(\phi_r \frac{\partial U_m}{\partial t} - \phi_r S_m - \frac{\partial \phi_r}{\partial x_i} F_{mi}\right) \mathrm{d}\Omega + \int_\Gamma \phi_r F_{mi}^* \mathrm{n}_i \mathrm{d}\Gamma = 0$$

where ϕ are the basis functions and the solution is approximated using $U_m = \phi_s a_{ms}$ where the index r and s run over the number of basis functions. The source term S_m only appears in the SA equation. The residual now contains integrals over faces Γ and special treatment is needed for the fluxes F_{mi}^* in these terms. The advective fluxes are calculated using any of the following choices: Lax-Friedrichs,[8] Roe,[9] and artificially upstream flux vector splitting scheme (AUFS).[10] The results in this paper use the Lax-Friedrichs flux and the diffusive fluxes are handled using a symmetric interior penalty (SIP) method.[11,12]

V. Solution Method

To solve the non-linear set of equations, a damped Newton-Rhapson method is used which has the form:

$$J^k_{mrns}\Delta a^k_{ns} = \left[\frac{\delta_{mn}M_{rs}}{\Delta t} + \frac{\partial R^k_{mr}}{\partial a^k_{ns}}\right]\Delta a^k_{ns} = -R^k_{mr} \tag{4}$$

where J_{mrns} is a block Jacobian matrix, k is the non-linear iteration, M_{rs} is a mass matrix and Δt is an element-wise time step which is used to dampen the solution.[4] The mass matrix M_{rs} is defined as:

$$M_{rs} = \int_\Omega \phi_r \phi_s \mathrm{d}\Omega$$

which, due to the discontinuous basis, only appears on the block diagonals. A local time step Δt is set on every element using

$$\Delta t = \frac{CFL}{h^{-1}(\sqrt{u^2+v^2+w^2}+c)}$$

where h is a mesh size and c is the speed of sound. The mesh size h is defined as:

$$h = \frac{V_{cell}}{A_{face}(p+1)^2},$$

where V_{cell} is the cell volume and A_{face} is the surface area of the faces on the cell. The CFL number is not based on an explicit stability limit, but rather is used to control the convergence characteristic of the implicit scheme.

The Newton-Rhapson method creates a linear system that must be solved to get the update to the coefficients a_{ns} by:

$$a^{k+1}_{ns} = a^k_{ns} + \Delta a^k_{ns}.$$

To solve the linear system in equation (4), a flexible-GMRES[13] (fGMRES) method is used. To further improve convergence of fGMRES a preconditioner can be applied to the system of equations. Preconditioners that have been implemented include Jacobi relaxation, Gauss-Seidel relaxation, line implicit Jacobi, and ILU(0).

VI. Problem Definition

A. Initial Conditions

The initial conditions are taken from the NASA turbulence modeling resource. The flow conditions are: angle of attack $\alpha = 10$, $Mach = 0.15$, $Re = 6 \times 10^6$, $\gamma = 1.4$, $Pr = 0.72$, and $Pr_t = 0.9$. The non-dimensional numbers are satisfied using the free stream conditions: $P_0 = 1/\gamma$, $\rho_0 = 1$, $U_\infty = 0.15$, $\mu_0 = 2.5 \times 10^{-7}$, and $\rho\nu_{t0} = \frac{3\mu_0}{\mu'}$ is the initial condition for the SA model transport equation.

B. Grids

The NASA turbulence modeling resource provides three families of grids. Results from FUN3D and CFL3D have shown that family II gives the most accurate answers. Therefore only family II grids will be used in these results. These grids have a farfield extent of approximately 500 chords, and the leading and trailing edge spacing is 1.25×10^{-5} chords. For the h-refinement study three grids are used: a quadrilateral mesh consisting of 1793×513 nodes, 897×257 nodes, and 449×129 nodes. For the p-refinement study only the 897×257 node grid is used. The quadrilateral grids are are extruded into the third dimension to create one layer of hexahedral elements.

C. Wall Distance

The wall distance is needed in the source term of the SA turbulence model transport equation and therefore shows up in integrals over the cell volume. The wall distance is computed in the beginning of the simulation at every cell quadrature point in the domain. For high order methods an accurate measurement of wall

distance is needed. To do this the airfoil top and bottom surfaces are defined using a large number of points (10^5) which are connected by straight lines. These points are found using the formula:

$$y = \pm 0.594689181\left(0.298222773\sqrt{x} - 0.127125232x - 0.357907906x^2 + 0.291984971x^3 - 0.105174606x^4\right),$$

which is the formula of a NACA 0012 airfoil modified to create a sharp trailing edge. The distance function is calculated at every quadrature point and is the minimum distance between this point and the straight lines defining the airfoil shape.

VII. Results

This section compares the DG results to the NASA turbulence modeling resource results for FUN3D and CFL3D. Both p-refinement and h-refinement simulations are perfomed without the point vortex correction. The p-refinement cases all use the 897×257 family II grid with polynomial degrees ranging from $p = 1$ to $p = 3$. The h-refinement cases all use a polynomial degree of $p = 1$ and three levels of grid refinement. In all of the following the degrees of freedom N for FUN3D and CFL3D are the total number of nodes. For the DG solver the total degrees of freedom are $N = n_{cell}(p+1)^2$ where n_{cell} are the total number of cells and p is the polynomial degree.

Figure 1 shows the drag coefficient for the DG solver, FUN3D, and CFL3D. The DG solver is converging to a slightly different value than FUN3D or CFL3D but is close to the range of acceptable values (represented by the green solid lines). We also note that p-refinement is converging faster than h-refinement. This is because with the same number of degrees of freedom a high order method gives more accurate results than a lower order method. Figure 2 shows the lift coefficient for all three methods. The DG solver is converging to a value very similar to FUN3D and is within the range of acceptable values. Again, p-refinement appears to be converging faster than h-refinement. Figure 3 shows the pitching moment coefficient. Again, the DG solver is converging to a value very similar to FUN3D and is within the range of acceptable values using p-refinement. The h refined solutions appear to be approaching the p refined results. Similar to previous results, p-refinement is converging faster than h-refinement.

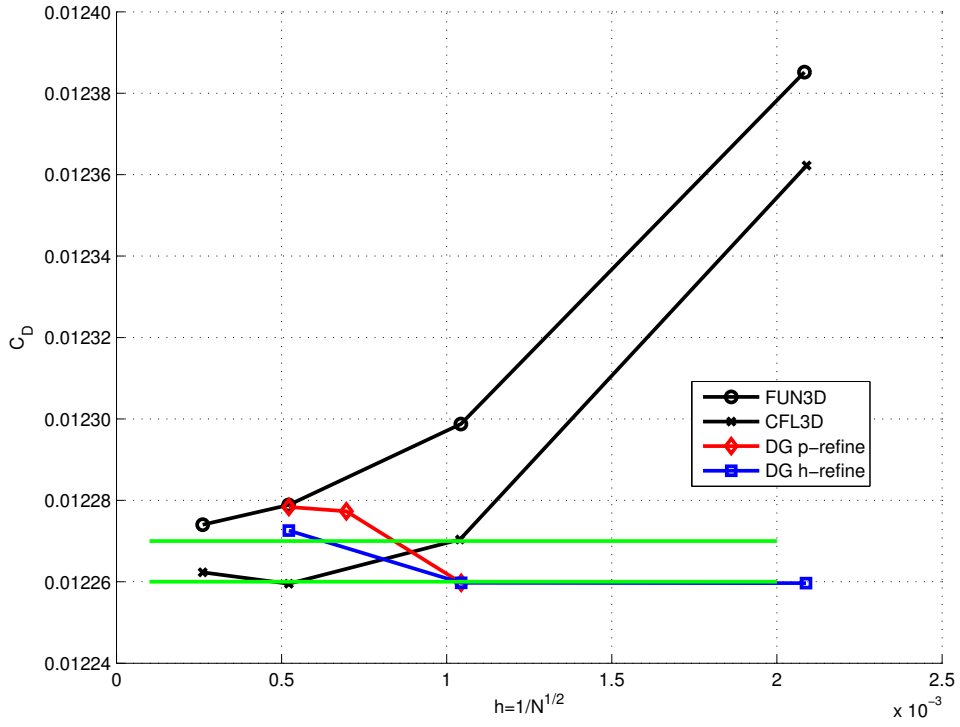

Figure 1. Drag coefficient for NACA 0012 at $\alpha = 10$, $Mach = 0.15$, and $Re = 6 \times 10^6$. Solid green lines are mesh converged result ranges.

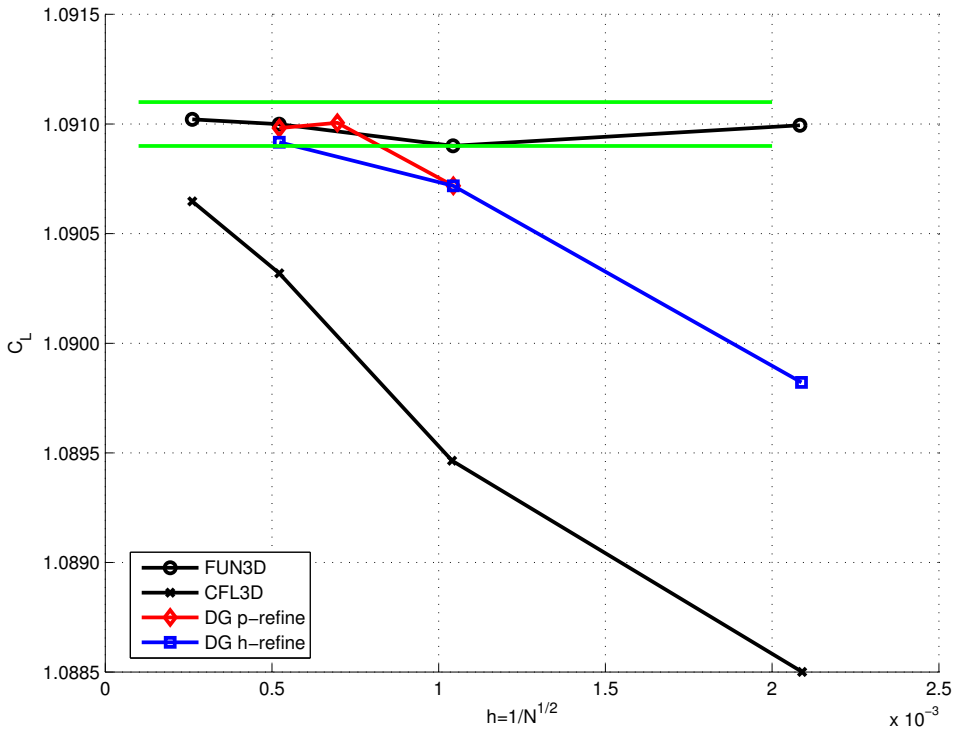

Figure 2. Lift coefficient for NACA 0012 at $\alpha = 10$, $Mach = 0.15$, and $Re = 6 \times 10^6$. Solid green lines are mesh converged result ranges.

The computed surface pressure coefficients (C_P) are shown in Figure 4, where they are compared with the FUN3D and CFL3D results for the finest family II grid with 7169×2049 nodes. The DG solver results are shown only for the family II grid with 897×257 nodes and polynomial degrees in the range of $p = 1$ to $p = 3$. At this scale all of the solutions appear to be identical. Figure 5 and Figure 6 show a close up of the computed results in the leading edge upper surface region. The $p = 1$ solution shows the large jumps in C_P distribution in this region. The $p = 2$ solution and $p = 3$ simulations are approaching a solution in-between the FUN3D and CFL3D solutions. A look at the trailing edge shown in Figure 7 and Figure 8 shows relatively large variations at every polynomial degree. However, the magnitude of the variations are exaggerated due to the scale of the plot.

The computed surface skin friction coefficient is shown in Figure 9, where they are compared with FUN3D and CFL3D results for the finest family II grid with 7169×2049 nodes. The DG solver results are shown only for the family II grid with 897×257 nodes and polynomial degrees in the range of $p = 1$ to $p = 3$. At this scale all of the solutions appear to be identical. Figure 10 and Figure 11 show a close up of the leading edge upper surface region. As the polynomial degree increases the solutions approach a mesh converged solution. However all of the DG solutions are slightly below the FUN3D and CFL3D results. A look at the trailing edge region shown in Figure 12 and Figure 13 shows relatively large variations at every polynomial degree.

Downstream from the airfoil Figure 14 shows the x-velocity along $x = 10/c$ with large variations between different resolutions. Only the finest FUN3D case and the $p = 3$ DG case give reasonable results. Within the DG cases: the finest mesh (1793×513) with a polynomial degree of $p = 1$ has the same degrees of freedom as a coarser mesh (897×257) with a polynomial degree of $p = 3$, however the $p = 3$ case gives better results. Figure 15 and Figure 16 along $x = 0.999/c$, Figure 17 along $x = 1.001/c$, and Figure 18 along $z = 0$ give very close x-velocity results for all cases. Figure 19 shows the x-velocity profile along $z = 0.00008/c$ and only shows slight discrepancies for the two coarsest DG cases.

Figure 20 shows the z-velocity along $x = 10/c$ with large variations between different resolutions. Similar to the x-velocity only the finest FUN3D case and the $p = 3$ DG case give reasonable results and the $p = 3$ DG case giving better results than a finer $p = 1$ DG case. Figures 21 and 22 along $x = 0.999/c$, Figure 23

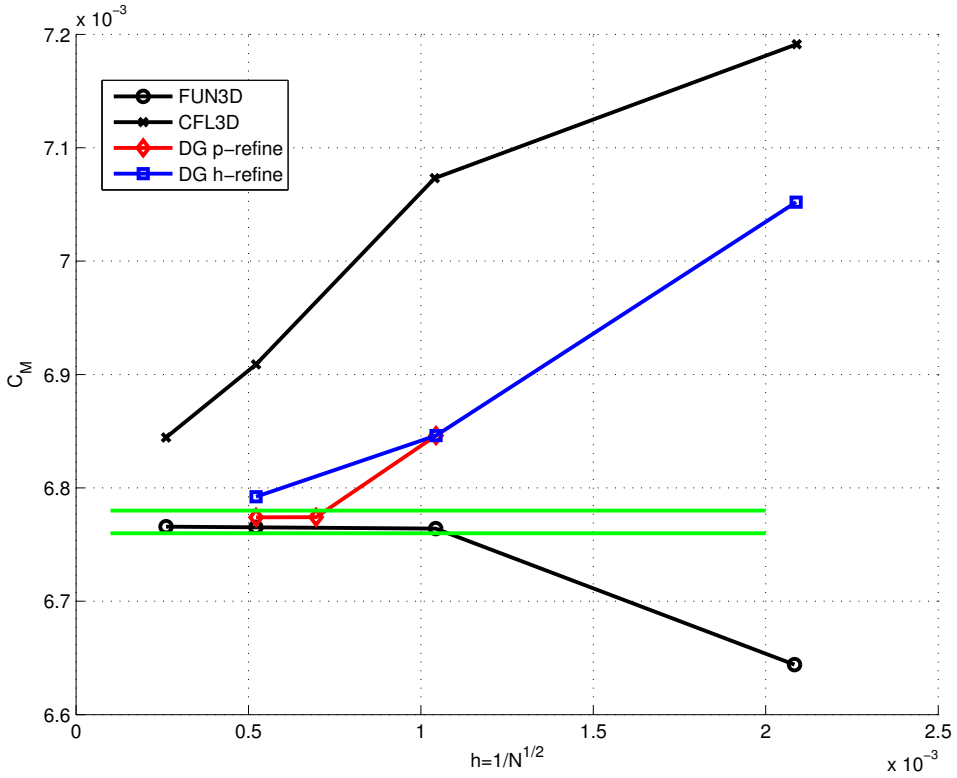

Figure 3. Pitching moment coefficient for NACA 0012 at $\alpha = 10$, $Mach = 0.15$, and $Re = 6 \times 10^6$. Solid green lines are mesh converged result ranges.

along $x = 1.001/c$, Figure 24 along $z = 0$, and Figure 25 along $z = 0.00008/c$ give very close z-velocity results for all cases except for the coarsest $p = 1$ DG case, which shows slight variations compared the more resolved cases.

Figure 26 and Figure 27 show the coefficient of pressure along $x = 0.999/c$. The coarse DG cases show large fluctuations and jumps. The higher resolution cases are smoother and are showing only slightly different results than the most resolved FUN3D case. Figure 28 shows coefficient of pressure along $x = 1.001/c$ and Figure 29 along $z = 0$ with good agreement to FUN3D except for the coarsest DG case. Figure 30 shows large fluctuations for coefficient of pressure along $z = 0.00008/c$ for most DG cases although this is due to the scale of the plot.

Figure 31 shows the dynamic eddy viscosity along $x = 10/c$ with large variations between different resolutions. Similar to before only the finest FUN3D case and the $p = 3$ DG case give reasonable results and the $p = 3$ DG case giving better results than a finer $p = 1$ DG case. Figure 32 and Figure 33 along $x = 0.999/c$, Figure 34 along $x = 1.001/c$, and Figure 35 along $z = 0$ give very close dynamic eddy viscosity results for all cases except for the coarsest $p = 1$ DG case, which shows slight variations compared the more resolved cases. Figure 36 along $z = 0.00008/c$ shows dynamic eddy viscosity converging to slightly different values than FUN3D.

VIII. Conclusions

In this work mesh resolved simulations are performed of the NACA 0012 airfoil. The NASA turbulence modeling resource website provides grids and reference solutions for the FUN3D and CFL3D solvers. These solutions are compared to DG simulations without the point vortex correction using a p-refinement study and a h-refinement study. In most cases the results match more closely to FUN3D. This is probably due to FUN3D using the same negative variant of the Spalart-Allmaras model as the DG solver. The drag coefficient appears to be converging to a slightly different value than FUN3D but is still very close to the

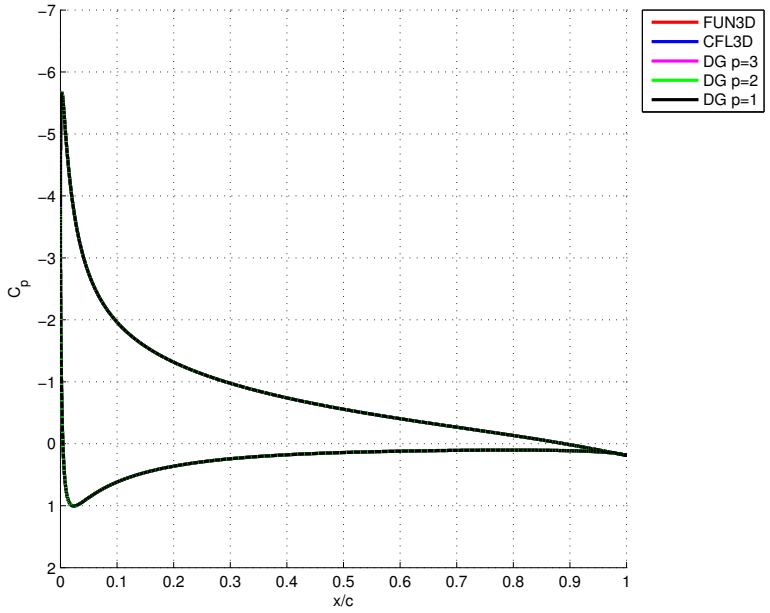

Figure 4. Computed surface pressure coefficient distribution for NACA 0012 at $\alpha = 10$, $Mach = 0.15$, and $Re = 6 \times 10^6$.

acceptable range. Both lift and pitching moment are within the acceptable range of values. For these cases the p-refinement cases converge more quickly than the h-refinement cases. This is because high-order methods provide more accurate results compared to lower-order methods for equivalent number of degrees of freedom. The pressure and skin friction coefficients on the surface of the airfoil also match closely to the FUN3D and CFL3D results. Only at the finest scales do discrepancies show up. To conclude, the DG solver provides consistent results to FUN3D and CFL3D and mesh resolved solutions are found. Also, higher- order methods converge to the mesh resolved solutions faster than mesh refinement alone.

References

[1]Reed, W. H. and Hill, T. R., "Triangular Mesh Methods for the Neutron Transport Equation," Tech. Rep. LA-UR-73-479, Los Alamos Scientific Laboratory, 1973.

[2]Persson, P.-O. and Peraire, J., "Sub-cell shock capturing for discontinuous Galerkin methods," *Collection of Technical Papers - 44th AIAA Aerospace Sciences Meeting*, Vol. 2, 2006, pp. 1408 – 1420.

[3]Barter, G. and Darmofal, D., "Shock capturing with PDE-based artificial viscosity for DGFEM: Part I. Formulation," *J. Comput. Phys. (USA)*, Vol. 229, No. 5, 2010/03/01, pp. 1810 – 27.

[4]Burgess, N. K. and Mavriplis, D. J., "An hp-adaptive discontinuous galerkin solver for aerodynamic flows on mixed-element meshes," *49th AIAA Aerospace Sciences Meeting Including the New Horizons Forum and Aerospace Exposition*, 2011.

[5]Brazell, M. J. and Mavriplis, D. J., *3D Mixed Element Discontinuous Galerkin with Shock Capturing*, American Institute of Aeronautics and Astronautics, 2014/12/03 2013.

[6]Allmaras, S., Johnson, F., and Spalart, P., "Modifications and Clarifications for the Implementation of the Spalart-Allmaras Turbulence Model," *7th International Conference on Computational Fluid Dynamics*, 2012.

[7]Ceze, M. and Fidkowski, K., *Pseudo-transient Continuation, Solution Update Methods, and CFL Strategies for DG Discretizations of the RANS-SA Equations*, American Institute of Aeronautics and Astronautics, 2014/12/05 2013.

[8]Lax, P. D., "Weak solutions of nonlinear hyperbolic equations and their numerical computation," *Communications on Pure and Applied Mathematics*, Vol. 7, No. 1, 1954, pp. 159–193.

[9]Roe, P., "Approximate Riemann solvers, parameter vectors, and difference schemes," *J. Comput. Phys. (USA)*, Vol. 43, No. 2, 1981/10/, pp. 357 – 72.

[10]Sun, M. and Takayama, K., "An artificially upstream flux vector splitting scheme for the Euler equations," *J. Comput. Phys. (USA)*, Vol. 189, No. 1, 2003/07/20, pp. 305 – 29.

[11]Hartmann, R. and Houston, P., "An optimal order interior penalty discontinuous Galerkin discretization of the compressible Navier-Stokes equations," *J. Comput. Phys. (USA)*, Vol. 227, No. 22, 2008/11/20, pp. 9670 – 85.

[12]Shahbazi, K., Mavriplis, D., and Burgess, N., "Multigrid algorithms for high-order discontinuous Galerkin discretizations of the compressible Navier-Stokes equations," *J. Comput. Phys. (USA)*, Vol. 228, No. 21, 2009/11/20, pp. 7917 – 40.

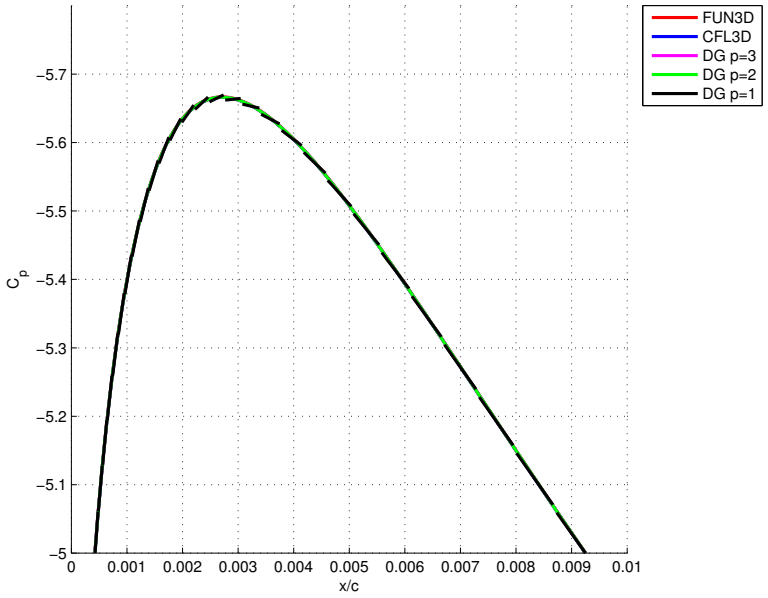

Figure 5. Details of computed surface pressure coefficient distribution in the leading edge region for NACA 0012 at $\alpha = 10$, $Mach = 0.15$, and $Re = 6 \times 10^6$.

[13]Saad, Y., "A flexible inner-outer preconditioned GMRES algorithm," *SIAM J. Sci. Comput.*, Vol. 14, No. 2, March 1993, pp. 461–469.

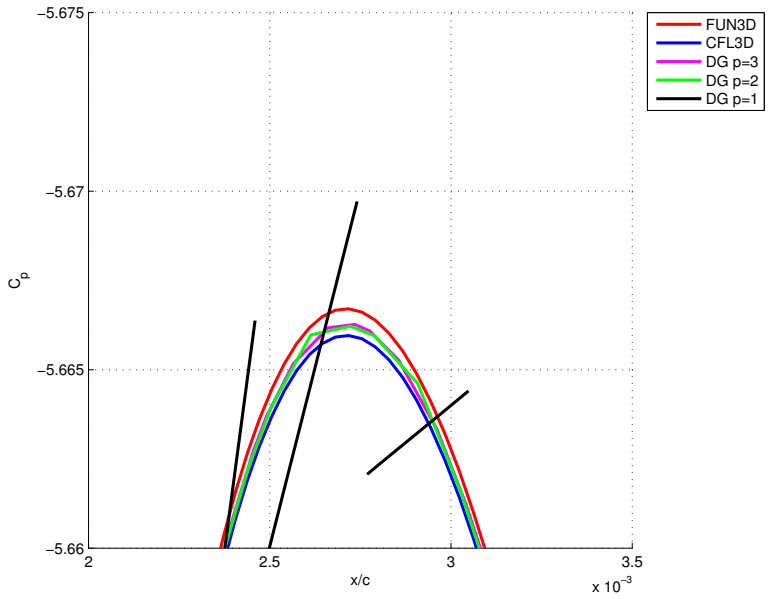

Figure 6. Details of computed surface pressure coefficient distribution in the leading edge region for NACA 0012 at $\alpha = 10$, $Mach = 0.15$, and $Re = 6 \times 10^6$.

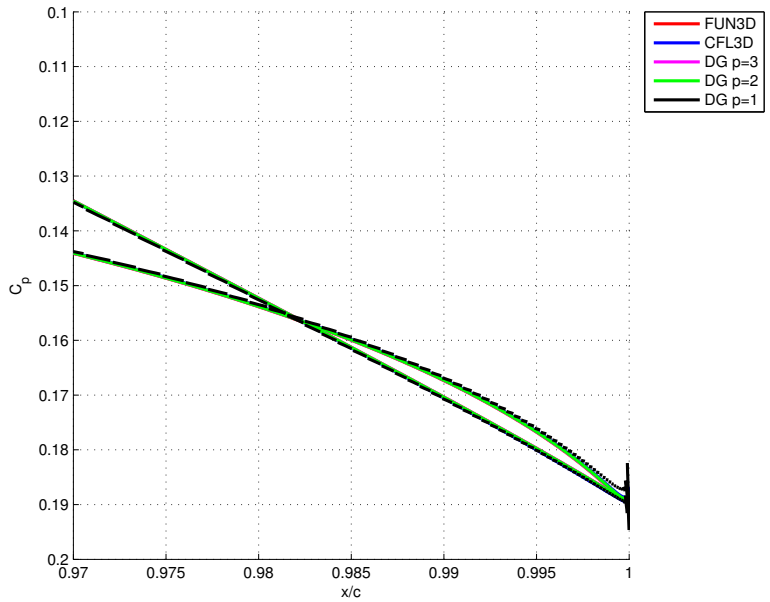

Figure 7. Details of computed surface pressure coefficient distribution in the trailing edge region for NACA 0012 at $\alpha = 10$, $Mach = 0.15$, and $Re = 6 \times 10^6$.

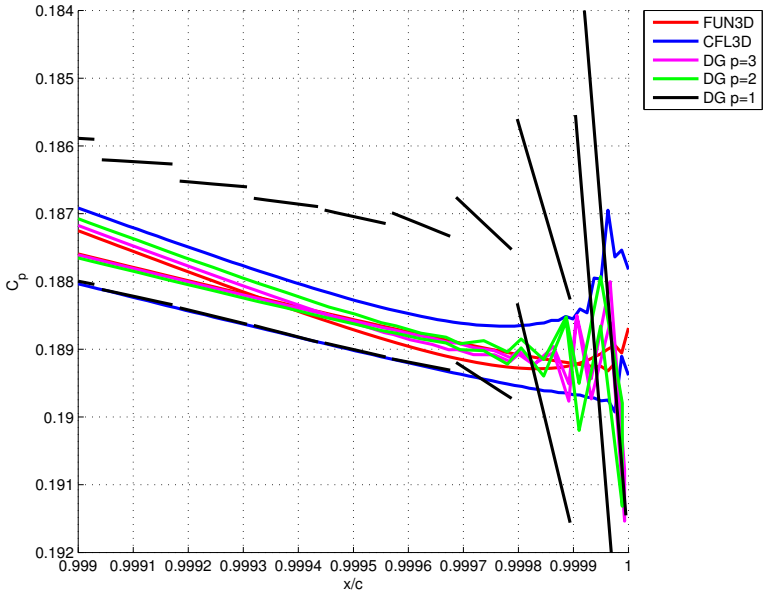

Figure 8. Details of computed surface pressure coefficient distribution in the trailing edge region for NACA 0012 at $\alpha = 10$, $Mach = 0.15$, and $Re = 6 \times 10^6$.

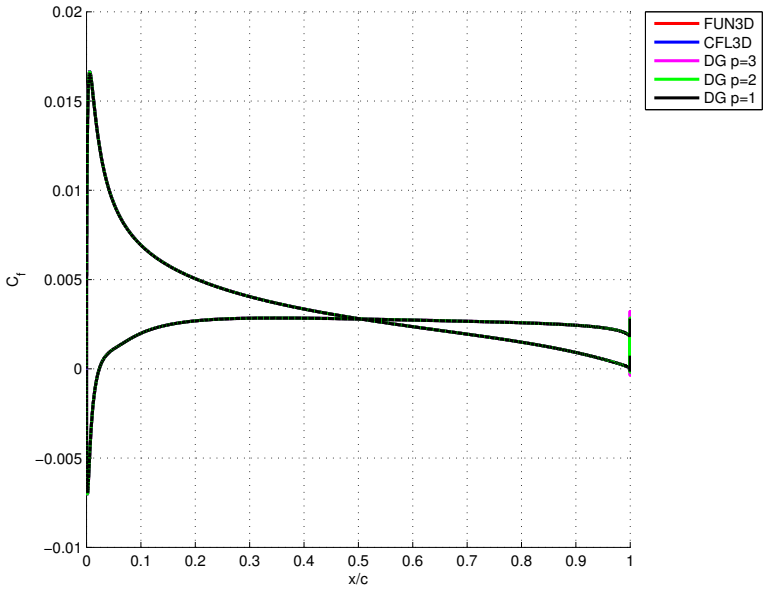

Figure 9. Computed surface skin friction coefficient for NACA 0012 at $\alpha = 10$, $Mach = 0.15$, and $Re = 6 \times 10^6$.

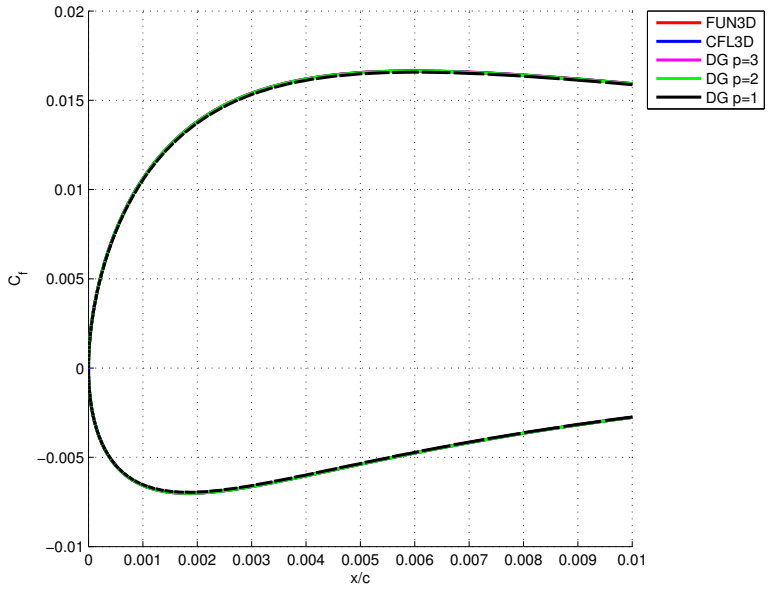

Figure 10. Details of computed Surface skin friction coefficient distributions in the leading edge region for NACA 0012 at $\alpha = 10$, $Mach = 0.15$, and $Re = 6 \times 10^6$.

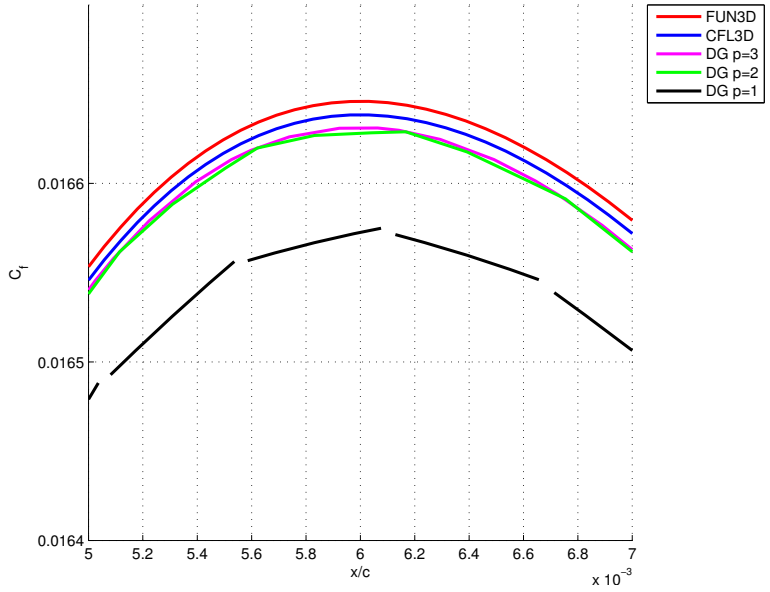

Figure 11. Details of computed Surface skin friction coefficient distributions in the leading edge region for NACA 0012 at $\alpha = 10$, $Mach = 0.15$, and $Re = 6 \times 10^6$.

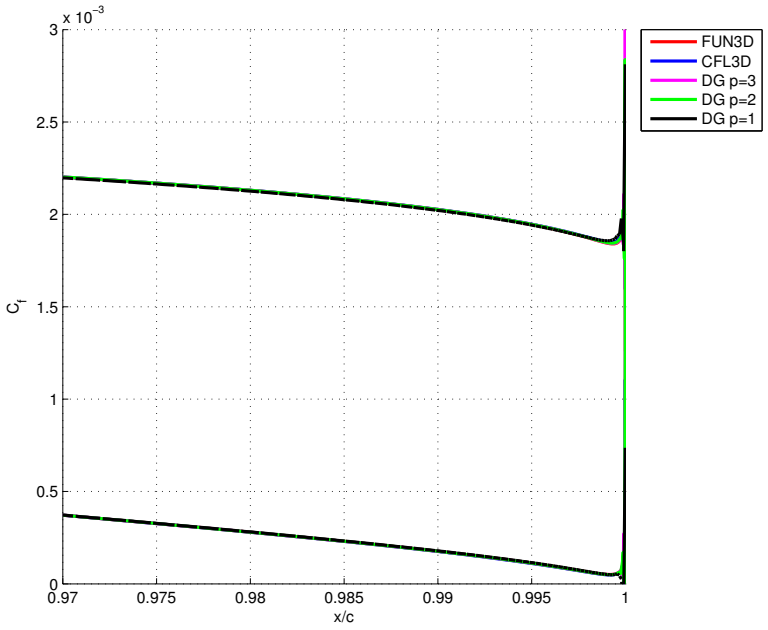

Figure 12. Details of computed Surface skin friction coefficient distributions in the trailing edge region for NACA 0012 at $\alpha = 10$, $Mach = 0.15$, and $Re = 6 \times 10^6$.

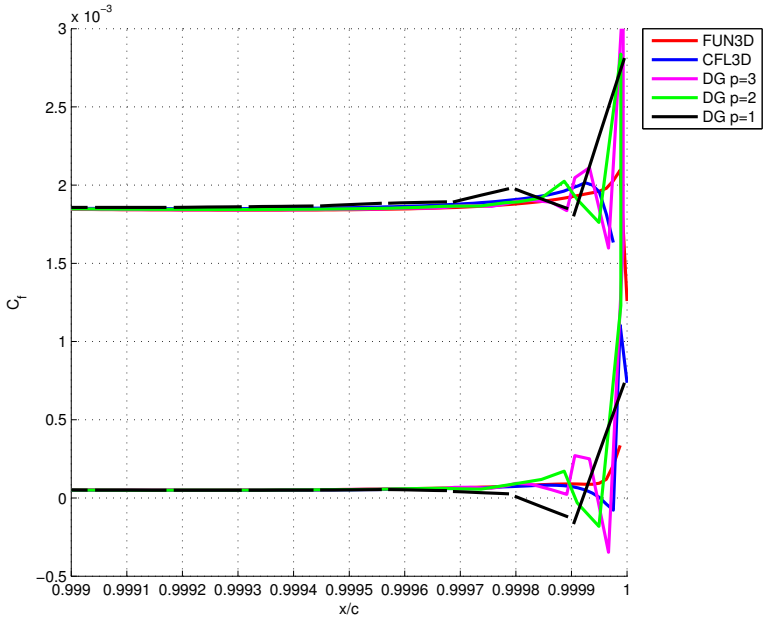

Figure 13. Details of computed Surface skin friction coefficient distributions in the trailing edge region for NACA 0012 at $\alpha = 10$, $Mach = 0.15$, and $Re = 6 \times 10^6$.

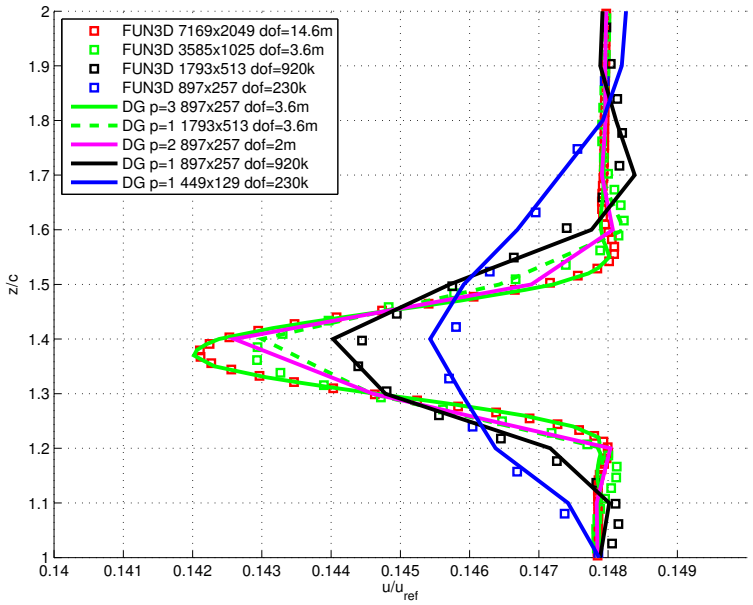

Figure 14. Velocity in x-dir along $x = 10/c$ for NACA 0012 at $\alpha = 10$, $Mach = 0.15$, and $Re = 6 \times 10^6$.

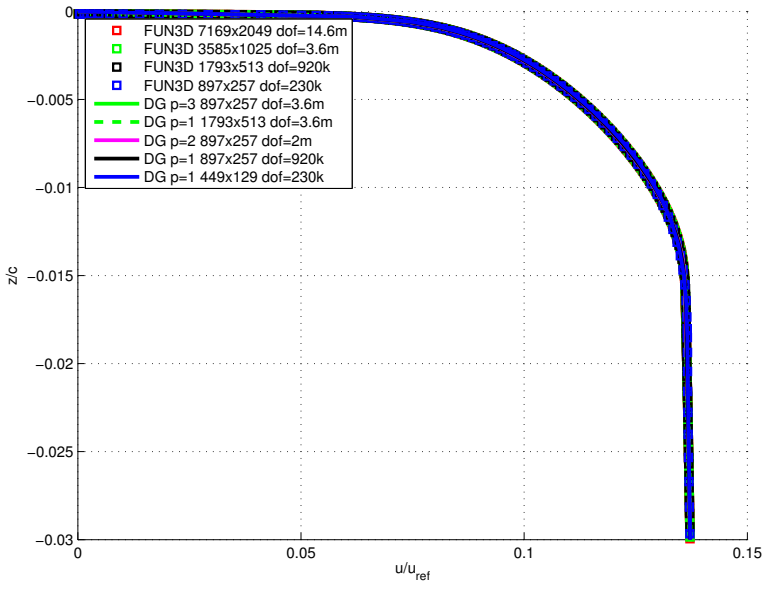

Figure 15. Velocity in x-dir along $x = 0.999/c$ (lower) for NACA 0012 at $\alpha = 10$, $Mach = 0.15$, and $Re = 6 \times 10^6$.

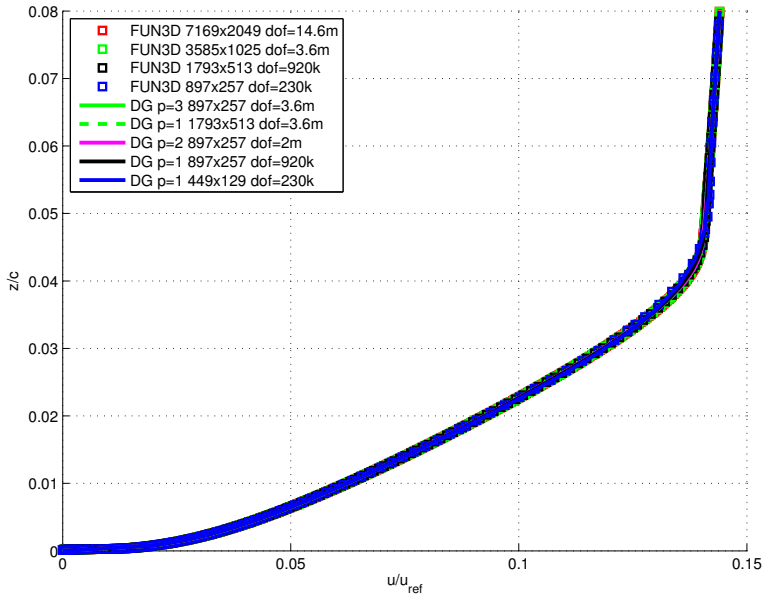

Figure 16. Velocity in x-dir along $x = 0.999/c$ (upper) for NACA 0012 at $\alpha = 10$, $Mach = 0.15$, and $Re = 6 \times 10^6$.

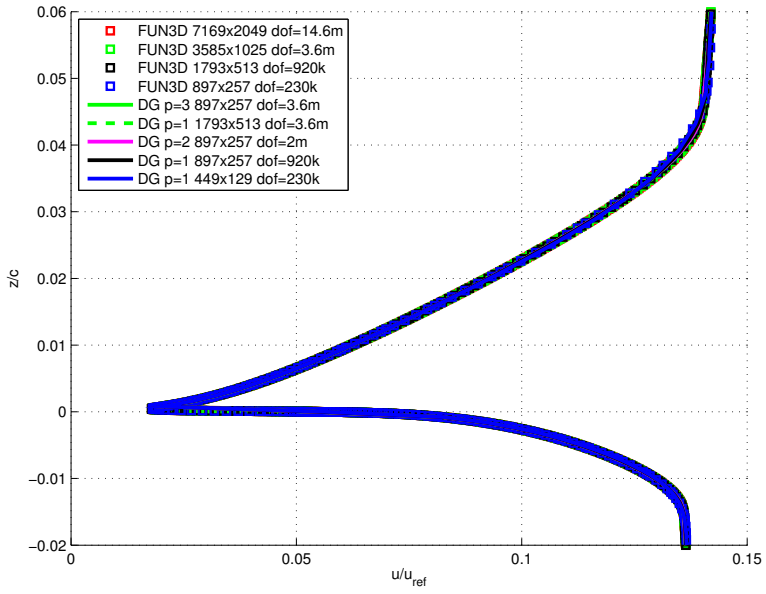

Figure 17. Velocity in x-dir along $x = 1.001/c$ for NACA 0012 at $\alpha = 10$, $Mach = 0.15$, and $Re = 6 \times 10^6$.

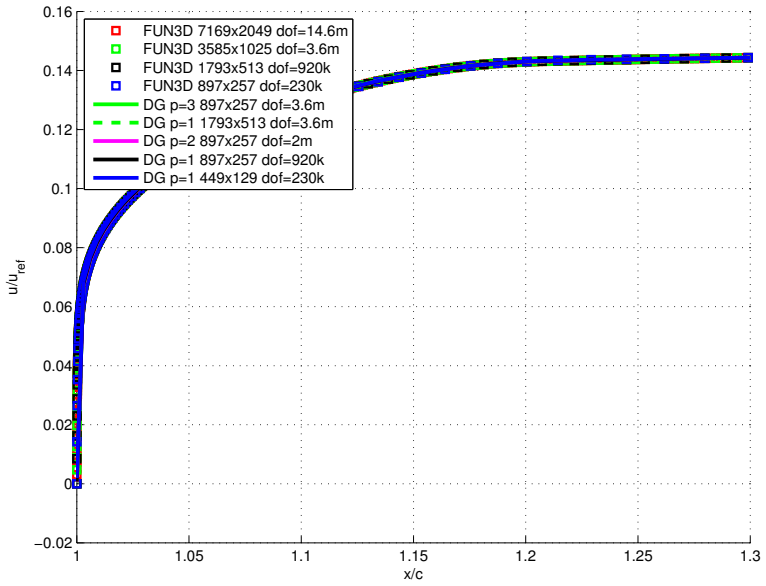

Figure 18. Velocity in x-dir along $z = 0$ for NACA 0012 at $\alpha = 10$, $Mach = 0.15$, and $Re = 6 \times 10^6$.

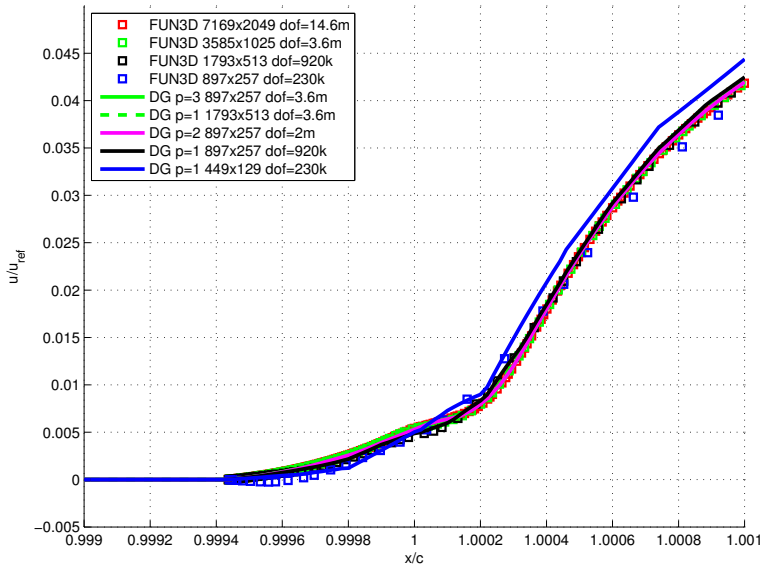

Figure 19. Velocity in x-dir along $z = 0.00008/c$ for NACA 0012 at $\alpha = 10$, $Mach = 0.15$, and $Re = 6 \times 10^6$.

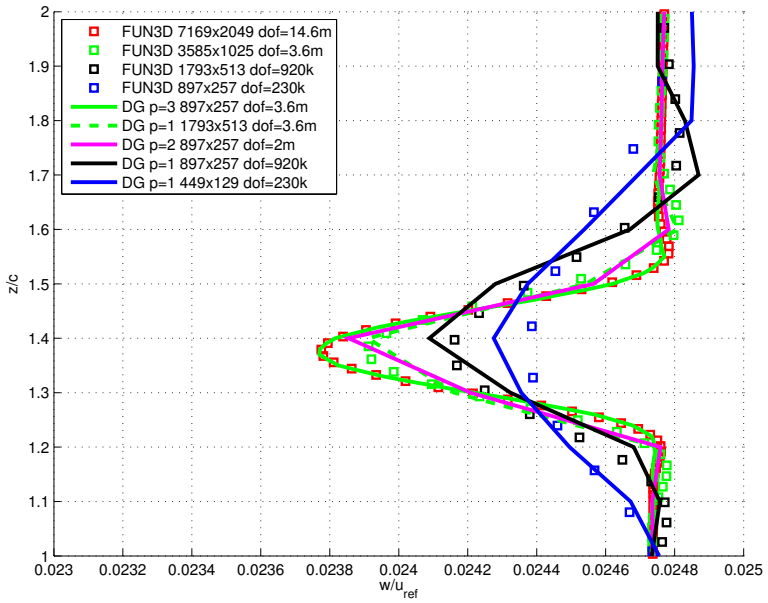

Figure 20. Velocity in z-dir along $x = 10/c$ for NACA 0012 at $\alpha = 10$, $Mach = 0.15$, and $Re = 6 \times 10^6$.

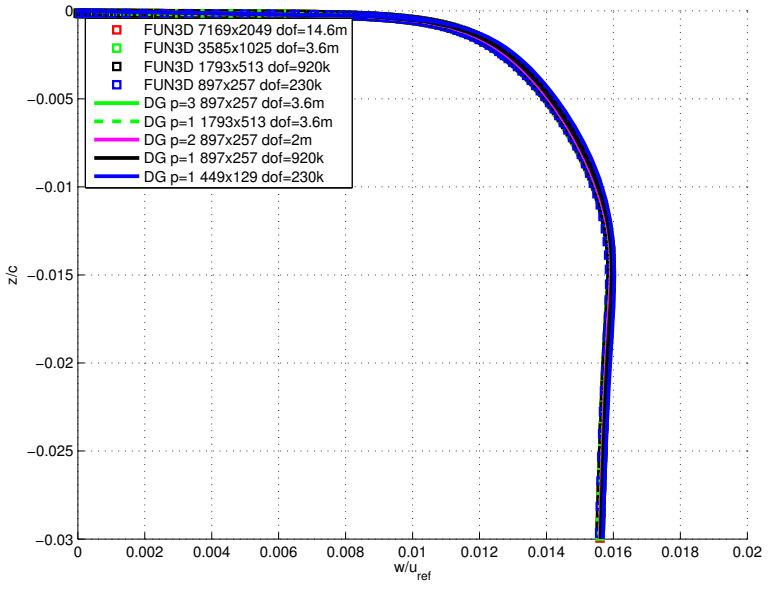

Figure 21. Velocity in z-dir along $x = 0.999/c$ (lower) for NACA 0012 at $\alpha = 10$, $Mach = 0.15$, and $Re = 6 \times 10^6$.

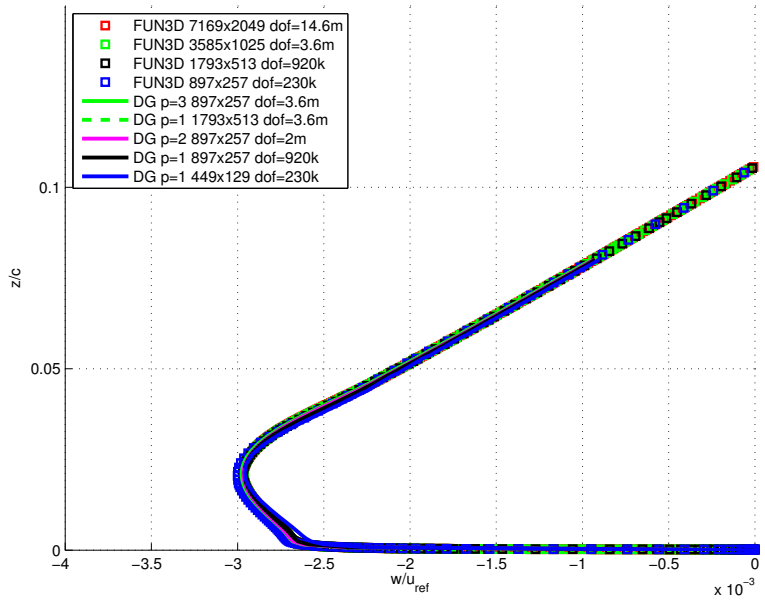

Figure 22. Velocity in z-dir along $x = 0.999/c$ (upper) for NACA 0012 at $\alpha = 10$, $Mach = 0.15$, and $Re = 6 \times 10^6$.

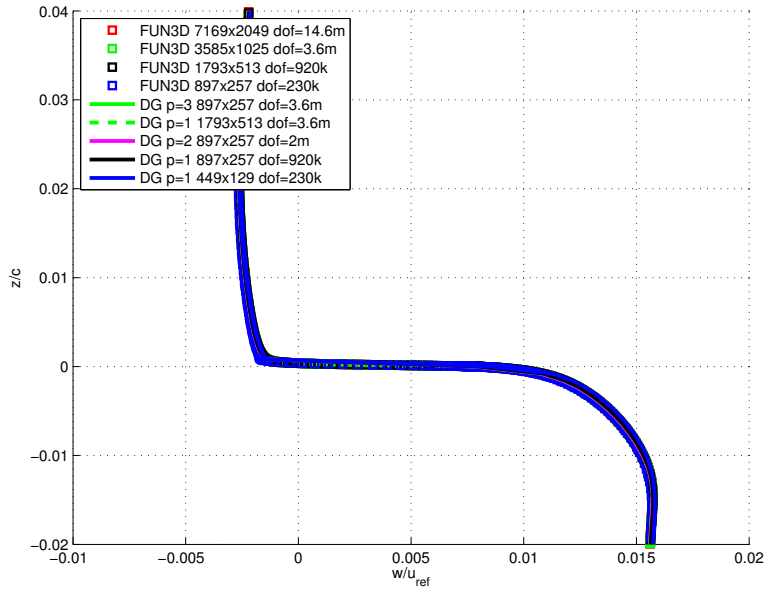

Figure 23. Velocity in z-dir along $x = 1.001/c$ for NACA 0012 at $\alpha = 10$, $Mach = 0.15$, and $Re = 6 \times 10^6$.

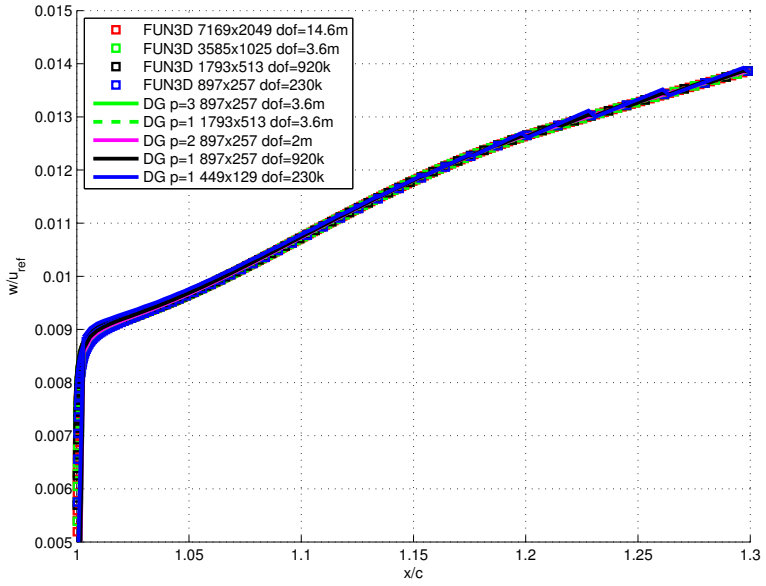

Figure 24. Velocity in z-dir along $z = 0$ for NACA 0012 at $\alpha = 10$, $Mach = 0.15$, and $Re = 6 \times 10^6$.

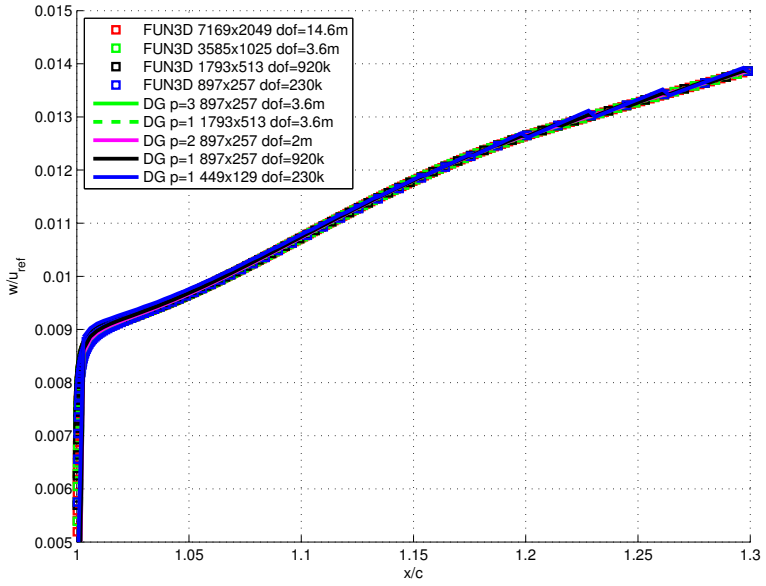

Figure 25. Velocity in z-dir along $z = 0.00008/c$ for NACA 0012 at $\alpha = 10$, $Mach = 0.15$, and $Re = 6 \times 10^6$.

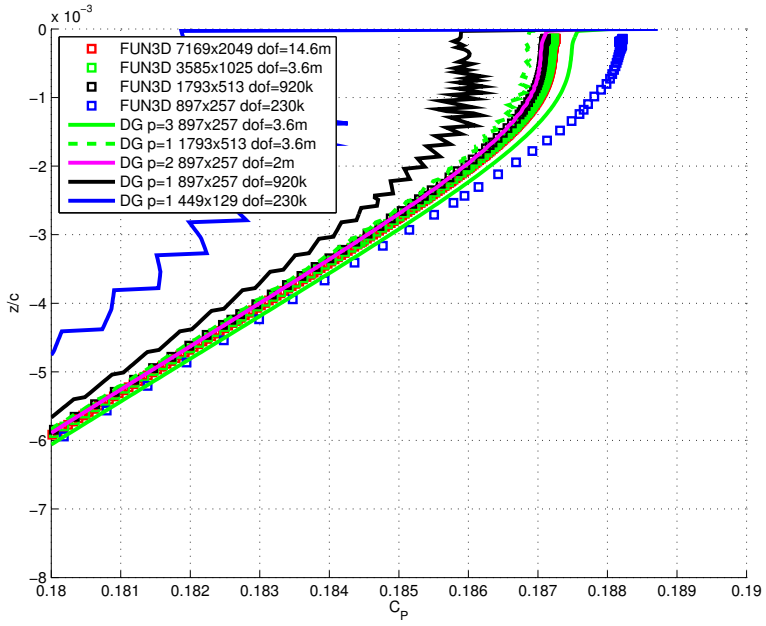

Figure 26. Coefficient of pressure along $x = 0.999/c$ (lower) for NACA 0012 at $\alpha = 10$, $Mach = 0.15$, and $Re = 6 \times 10^6$.

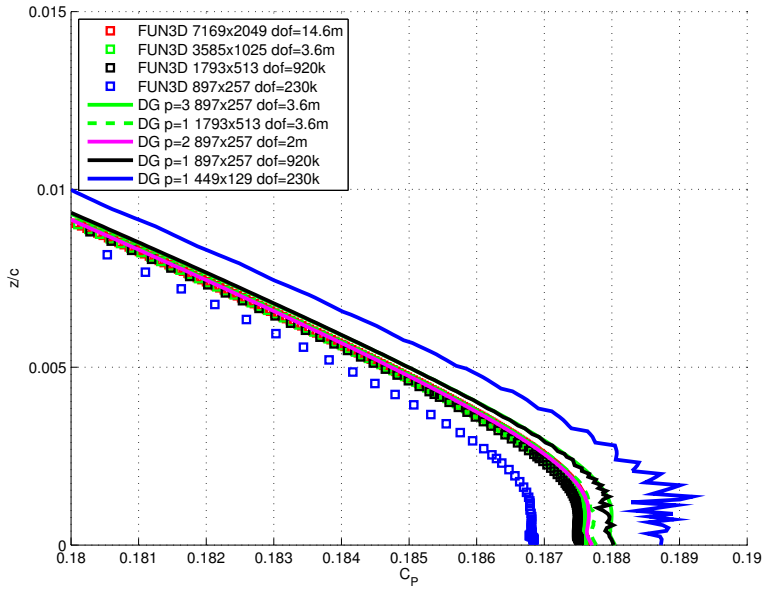

Figure 27. Coefficient of pressure along $x = 0.999/c$ (upper) for NACA 0012 at $\alpha = 10$, $Mach = 0.15$, and $Re = 6 \times 10^6$.

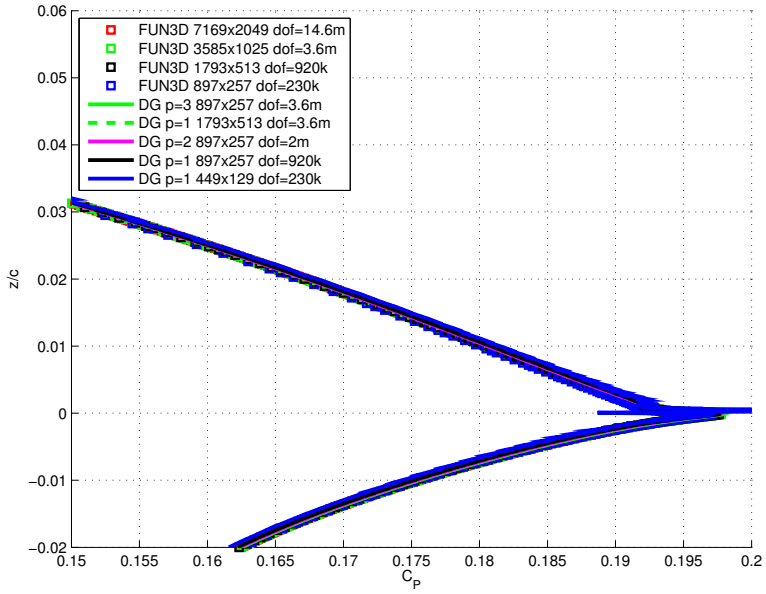

Figure 28. Coefficient of pressure along $x = 1.001/c$ for NACA 0012 at $\alpha = 10$, $Mach = 0.15$, and $Re = 6 \times 10^6$.

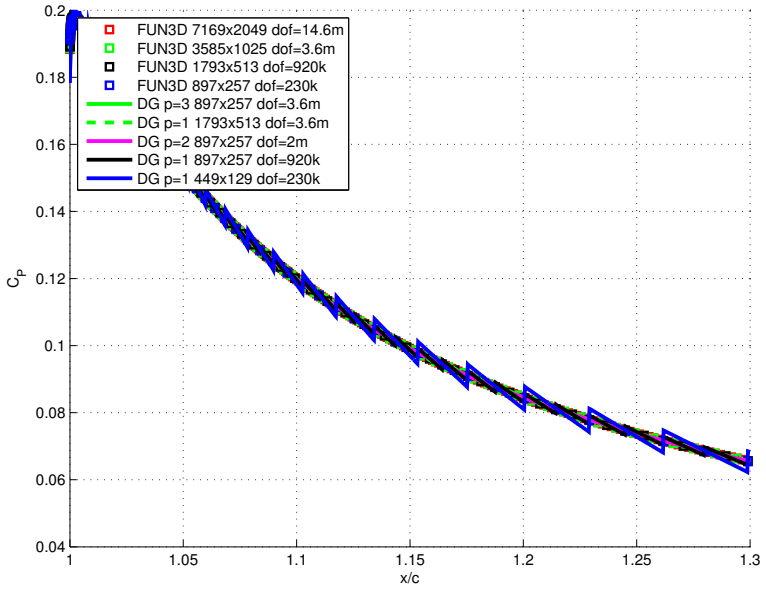

Figure 29. Coefficient of pressure along $z = 0$ for NACA 0012 at $\alpha = 10$, $Mach = 0.15$, and $Re = 6 \times 10^6$.

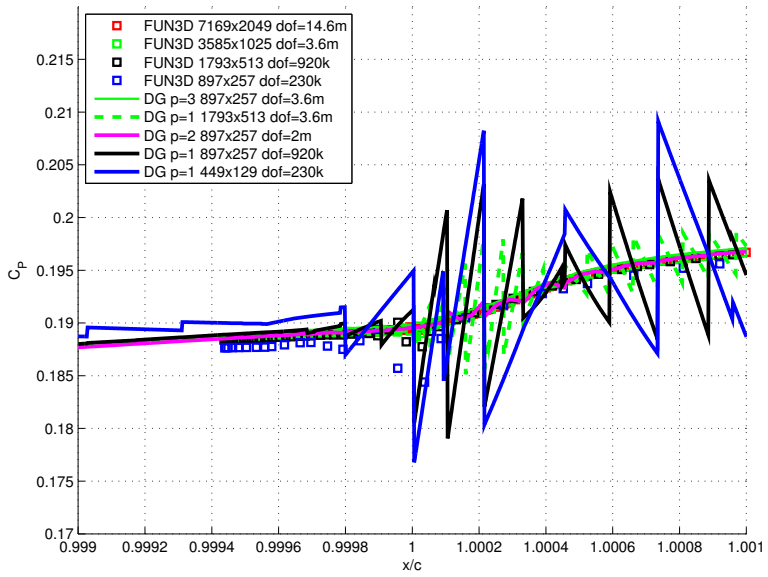

Figure 30. Coefficient of pressure along $z = 0.00008/c$ for NACA 0012 at $\alpha = 10$, $Mach = 0.15$, and $Re = 6 \times 10^6$.

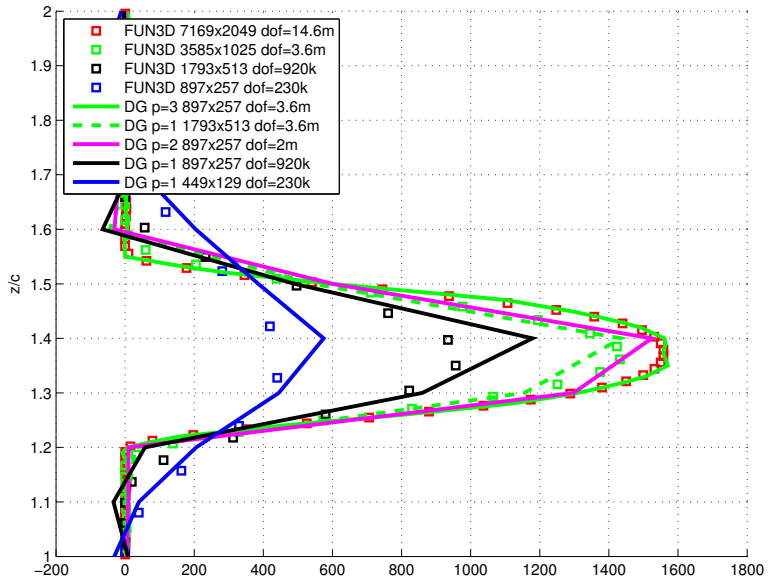

Figure 31. Dynamic eddy viscosity along $x = 10/c$ for NACA 0012 at $\alpha = 10$, $Mach = 0.15$, and $Re = 6 \times 10^6$.

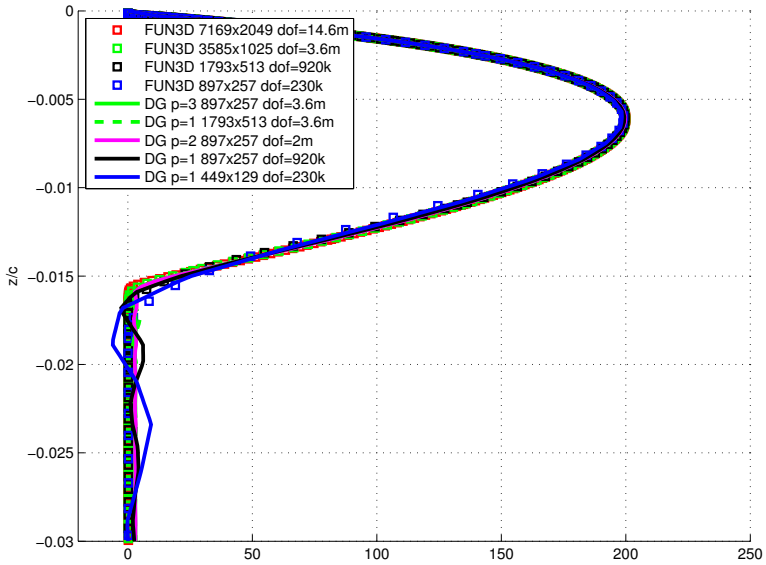

Figure 32. Dynamic eddy viscosity along $x = 0.999/c$ (lower) for NACA 0012 at $\alpha = 10$, $Mach = 0.15$, and $Re = 6 \times 10^6$.

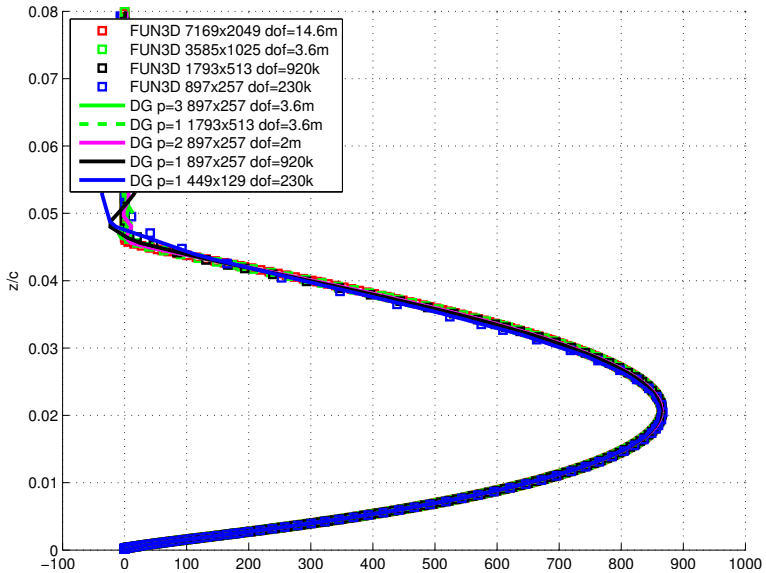

Figure 33. Dynamic eddy viscosity along $x = 0.999/c$ (upper) for NACA 0012 at $\alpha = 10$, $Mach = 0.15$, and $Re = 6 \times 10^6$.

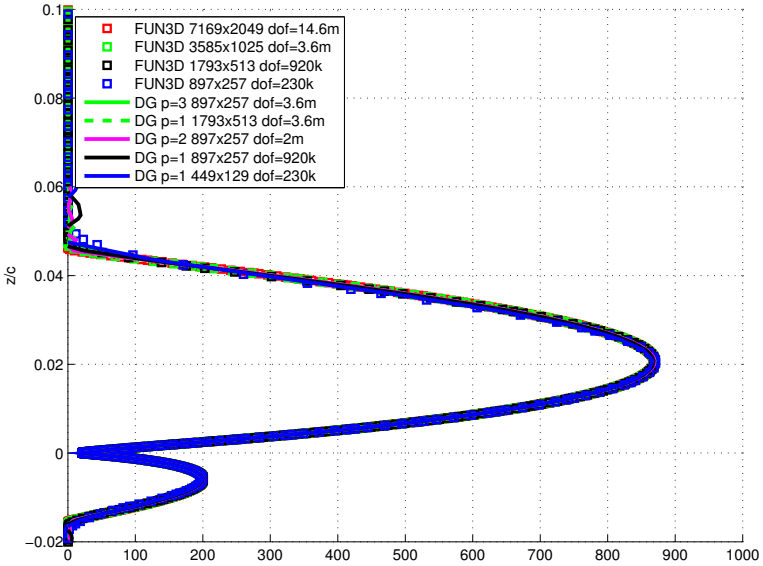

Figure 34. Dynamic eddy viscosity along $x = 1.001/c$ for NACA 0012 at $\alpha = 10$, $Mach = 0.15$, and $Re = 6 \times 10^6$.

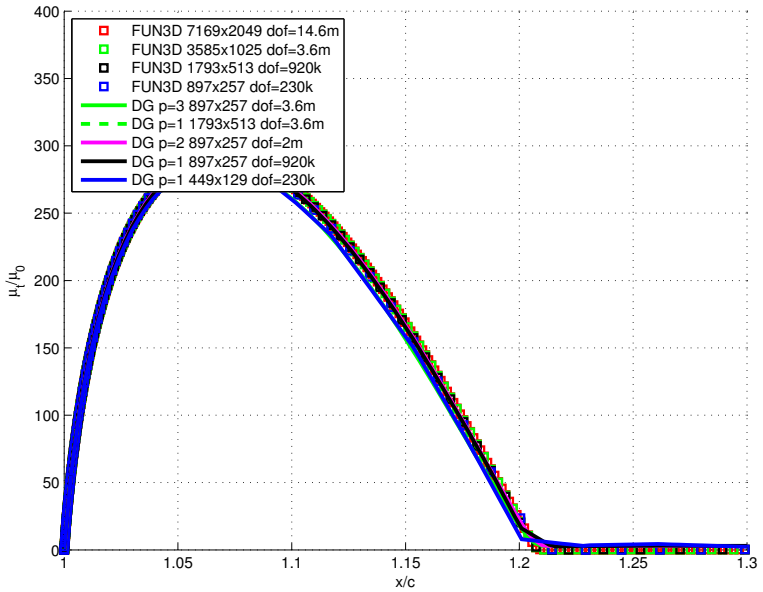

Figure 35. Dynamic eddy viscosity along $z = 0$ for NACA 0012 at $\alpha = 10$, $Mach = 0.15$, and $Re = 6 \times 10^6$.

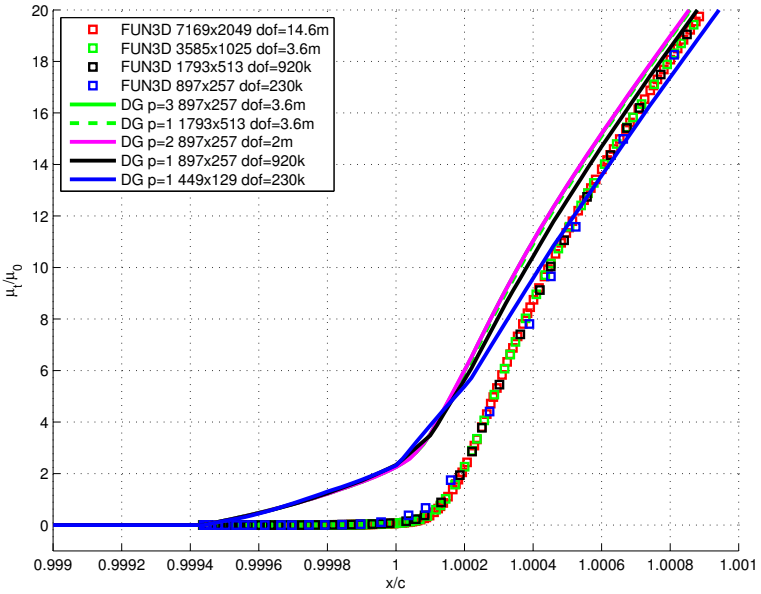

Figure 36. Dynamic eddy viscosity along $z = 0.00008/c$ for NACA 0012 at $\alpha = 10$, $Mach = 0.15$, and $Re = 6 \times 10^6$.